

Paper:

Multi-Temporal Correlation Method for Damage Assessment of Buildings from High-Resolution SAR Images of the 2013 Typhoon Haiyan

Pisut Nakmuenwai^{*,**}, Fumio Yamazaki^{*}, and Wen Liu^{*}

^{*}Graduate School of Engineering, Chiba University
1-33 Yayoi-cho, Inage-ku, Chiba 263-8522, Japan

^{**}Geo-Informatics and Space Technology Development Agency, Thailand
E-mail: pisut@gistda.or.th

[Received December 23, 2015; accepted April 2, 2016]

In this study, damage caused by Typhoon Haiyan in the city of Tacloban, Philippines is extracted from COSMO-SkyMed imagery data. A multitemporal correlation map, i.e., a color composite of the backscattering coefficients obtained on different days and their correlation coefficients, is used to indicate changes. The Hyperboloid Change Index is proposed as a measure of the level of destruction. The method is demonstrated in a three-dimensional Cartesian coordinate system to elaborate the relationships among the aforementioned parameters. Compared to other candidate methods, a hyperboloid equation is found to be the most suitable for change detection, and its resulting positive value indicates that the typhoon had a high level of impact on the area. Potential damage areas are extracted using a thresholding operation, and the results are compared to two WorldView-2 satellite images to specifically assess coastal erosion and damage to buildings and offshore fish traps.

Keywords: damage detection, multi-temporal SAR images, coherence, correlation coefficient

1. Introduction

In a SAR interferogram, the coherence (γ), which is derived by processing Single-Look Complex (SLC) co-registered data, is a measure of the correlation in a small neighborhood of geometric conditions. This value also indicates some specific information. A strong coherence implies that two images are homogenous, i.e., that the land surface has not changed and the geometric conditions are very similar. A weak coherence indicates that there has been a change due to one or more conditions, including a significant difference in look angles, constantly moving water surfaces, or land cover changes [1]. Therefore, SLC has been widely applied to land cover classification [2–5]. Furthermore, when used over a short time interval, it can distinguish between processes, such as manmade activities, moving objects, or damage detection [6–11].

Similar to the coherence, the correlation coefficient (R), which is more commonly used in statistics, is a measure of the linear correlation between two variables or pixel values in a local area from two images; the value of the correlation coefficient ranges from -1 and $+1$. The squared correlation coefficient of the SAR intensity has been proven to be a quick coherence estimator and is implemented in the same manner as coherence [12, 13]. Although the coherence and correlation coefficient are very similar in the sense that they provide a value for the correspondence between two time points, they detect different kinds of change on the ground. The coherence is influenced by the phase difference, which is specific to the spatial arrangement and thus to possible displacements. The intensity correlation is related to changes in the magnitude of the SAR backscatter, which in turn is related to the roughness permutation [14]. Some studies have shown that the aforementioned methods perform almost identically when identifying the major factor of the decorrelation [15]. However, some studies have determined that the normalized coherence is better suited to and more useful for damage assessment [16, 17]. Another study has found that the coherence is more useful for distinguishing slight to moderate damage levels, whereas the correlation coefficient is more sensitive to large surface changes [18]. In contrast, some studies have claimed that the correlation coefficient is slightly more sensitive to ground changes. Furthermore, a combination of both methods has slightly increased the overall accuracy [14].

Recent studies have primarily used the difference and coherence (or the correlation coefficient) to estimate the severity of damage caused by various natural hazards in several ways [19]. In this study, the same parameters are used for damage extraction but with a different concept that overcomes the deficiency of the degree of change not being able to be determined on one scale. A new technique is introduced that utilizes three change parameters instead of the more common one or two.

Because buildings are the most valuable assets of families and businesses, the assessment of the damage to buildings in typhoon events using high-resolution SAR images is a suitable topic of study. Among the types

Table 1. List of symbols and acronyms used throughout the text.

| Acronym | Meaning |
|------------|----------------------------------|
| σ^o | backscatter coefficient |
| ϕ | phase |
| γ | coherence |
| a | hyperboloid constant a |
| b | hyperboloid constant b |
| c | hyperboloid semi-major axis |
| d | subtraction |
| d' | normalized subtraction |
| s | addition |
| s' | normalized addition |
| A | amplitudes |
| C | complex number |
| D | difference |
| D' | normalized difference |
| D_{SD} | standard deviation D |
| S | summation |
| S' | normalized summation |
| S_{SD} | standard deviation S |
| R | correlation coefficient |
| R' | normalized R |
| R_{SD} | standard deviation R |
| R_C | combined correlation |
| H' | hyperboloid equation |
| Δd | absolute difference change index |
| Δw | weight method change index |
| Δr | cylindrical change index |
| Δh | hyperboloid change index |

of damage that occurs in natural disasters, the damage caused by winds is relatively easy to detect using satellite imagery because winds usually damage roofs. Furthermore, because there is a high probability of cloud cover, optical sensors are often not useful. For this reason, radar sensors are a better choice for rapid damage assessment. Although SARs operate in several frequency bands, the L, C and X bands are most often used. The X-band provides the highest spatial resolution; thus, it was most suitable for use in this study.

Typhoon Haiyan, which is known as Yolanda in the Philippines, was used in a case study. Considered to be the strongest tropical cyclone in recorded history, it struck land in the Philippines with a wind speed of 195 miles (314 km) per hour on November 8, 2013. The typhoon killed more than 6,300 people, displaced 16 million people, and did a total of PhP 89 billion (US\$ 2 billion) in damage [20]. In this study, the detection of damage to buildings was carried out using pre- and post-event COSMO-SkyMed (CSK) images, and the results were compared to the results of visual inspections of high-resolution optical satellite data. The new change index proposed in this study was designed to be suitable for detecting damage to buildings and determining the degree of change in general case between two SAR images.

The meanings of symbols and acronyms used in this article are listed in **Table 1**.

2. Study Area and Imagery Data

This paper focuses on Tacloban, which is the capital city of Leyte province and its surrounding areas on Leyte Island. Located 580 km southeast of Manila, Tacloban was struck by the eye wall, which was the most powerful part of the storm. The typhoon wrought massive destruction on the city. Widespread devastation was caused by the extreme winds, and lowlands on the eastern side of the city were submerged by storm surges. Because the city had a large population, the number of deaths there accounted for 48% (2,678) of the total deaths in the Philippines in this event [20]. After the super typhoon struck land, the storm surges and the extreme wind speeds were the major causes of damage. Strong waves and rising water levels, which were assumed to have heights of approximately 4 m, inundated and caused catastrophic damage to the coastal areas [21]. Tacloban’s airport was the area most affected due to its location; it was directly hit by the winds and surges. For these reasons, an area approximately 7.0 km wide and 12.3 km long (**Fig. 1**), an area which includes Tacloban’s downtown area, was selected as the study site.

The orbital parameters of CSK were favorable for multi-temporal image analyses. However, the two sets of imagery data were taken from different satellites and there were rather long time intervals between them. The pre-event image was taken by CSK-1 on August 7, 2013; the post-event image was taken by CSK-3 on November 20, 2013. The temporal baseline (Btemp) was 105 days, and the perpendicular baseline (Bperp) distance between the two satellite orbits was 885.2 m. The images were taken from the descending path with the right-looking HH polarization in the StripMap HIMAGE mode [22]. Both images have incidence angles between 44.99 and 47.19 degrees, and they have spatial resolution of 0.94 m in the azimuthal direction and 1.57 m in the range direction. The ground resolution was 2.18 m after orthorectification.

Two high-resolution optical satellite images acquired by WorldView-2 (WV-2) were also employed as ground truth data. The pre-event image was acquired on May 18 and the post-event image on November 11, 2013. Both images have 8 multispectral bands (2.0 m resolution) and a panchromatic band (0.5 m). After pansharpening using the Brovey technique, 0.5 m resolution multispectral images were prepared.

3. Change Detection Workflow

Radiometric calibration provides images in which pixels can be directly related to the radar backscatter of the scene by applying product factor corrections, e.g., the reference slant-range, reference incidence-angle, rescaling factor and the calibration factor. This process results in the backscattering coefficient, which is essential for the comparison of SAR images acquired by different sensors, by the same sensor at different times, or by the same sensor in different modes [23]. To use the backscattering co-

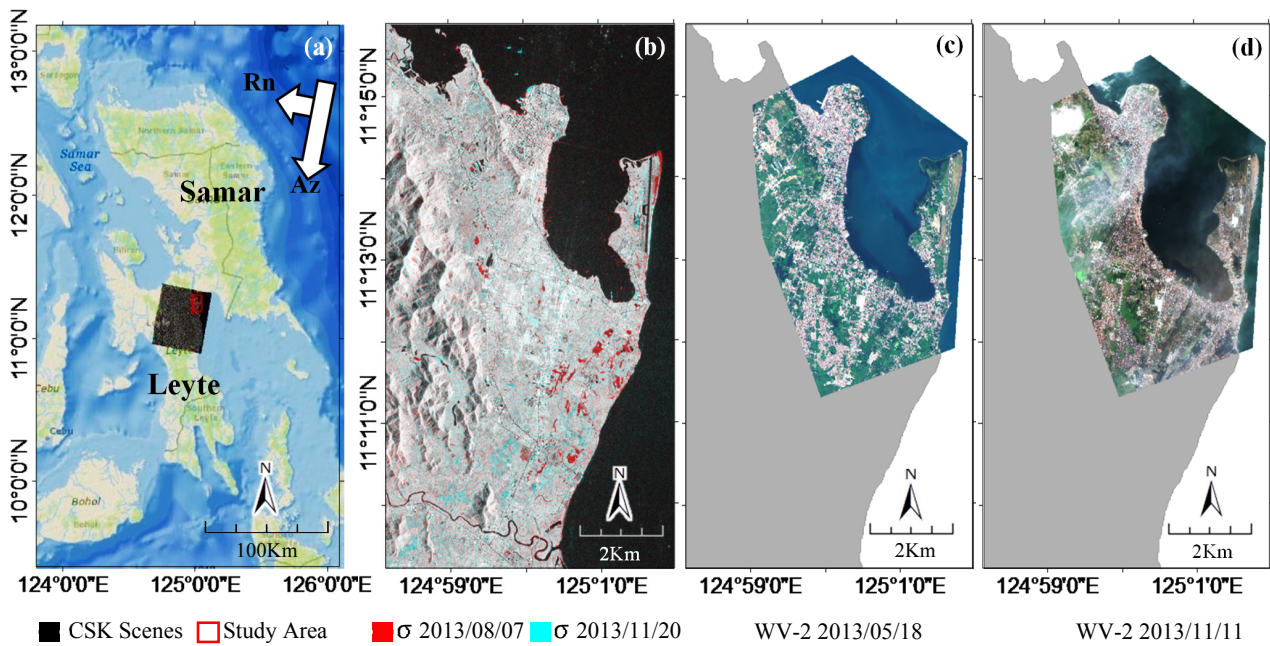


Fig. 1. (a) The footprint of the CSK scenes and Tacloban, Leyte study area. (b) Color composite of the pre- and post-event CSK backscattering coefficients. (c–d) True color composite of the pre- and post-event WV-2 images.

efficient (σ^o) for detecting surface changes, a calibration must first be applied to a pair of co-registered images. In a preliminary test, a window size of 5×5 was found to be suitable for the building damage detection. It was therefore adopted for both methods in the coherence and correlation coefficient calculations.

The MTC and MTR mapping methods were applied to evaluate the effects of the typhoon. Subsequently, SARBM3D filtering was applied to reduce the speckle while retaining the backscatter information [24]. An orthorectification using an SRTM 3 sec DEM was applied. This application was intended to compensate for distortions caused by topographical variations in the scene, to compensate for the tilt of the satellite, and to assign real-world coordinates to each pixel.

The change detection process was accomplished by calculating the difference and summation. Then, normalization was carried out on these values, including the correlation coefficient, before the change index was calculated. Finally, thresholding was applied by selecting the appropriate value regarding the pre- and post-event WV-2 images. An assessment of the accuracy was performed by comparing this result to the visualization of the WV-2 images. The two kinds of data were not compared directly but rather by using the final results as the extracted damage percentage. A flowchart of the processes is shown in Fig. 2.

3.1. Coherence (γ) and Correlation (R)

In repeat-pass interferometry, the coherence (γ) is derived from a pair of images in the same local area taken within a certain time-interval. The exact coherence and the relation between the interferometric phase dispersion

can be derived using a mathematical operation. Therefore, the coherence is frequently calculated as an estimator [25] using two co-registered single-look complex (SLC) images, as in Eq. (1):

$$\gamma = \frac{\sum C_1 C_2}{\sqrt{\sum |C_1|^2} \sqrt{\sum |C_2|^2}} \dots \dots \dots (1)$$

where C is a complex number with phase (ϕ) and amplitude (A) [26].

The Pearson correlation coefficient (R) is a measure of linear dependence and is defined as the covariance of two variables divided by the product of their standard deviations. In this case, it was calculated from the backscattering coefficients (σ^o) of the two images using Eq. (2) with a moving window. Because this statistic determines the linear trend, and the SAR intensity is distributed in an exponentially increasing manner, it was appropriate to use decibel units (dB), which are on a logarithmic scale.

$$R = \frac{\sum (\sigma_1^o - \bar{\sigma}_1^o)(\sigma_2^o - \bar{\sigma}_2^o)}{\sqrt{\sum (\sigma_1^o - \bar{\sigma}_1^o)^2} \sqrt{\sum (\sigma_2^o - \bar{\sigma}_2^o)^2}} \dots \dots (2)$$

3.2. MTC and MTR Visual Interpretation

For the MTC map shown in Fig. 3a, red is used for the amplitude of the pre-event (A_1), green for that of the post-event (A_2) and blue for their coherence (γ). For the MTR map shown in Fig. 3b, red is used for the backscattering coefficient of the pre-event (σ_1), green for that of the post-event (σ_2) and blue for their correlation coefficient (R). The color composite of the SAR images visually provides information on the increase/decrease of the backscattering intensity at different times. The interferometric coherence

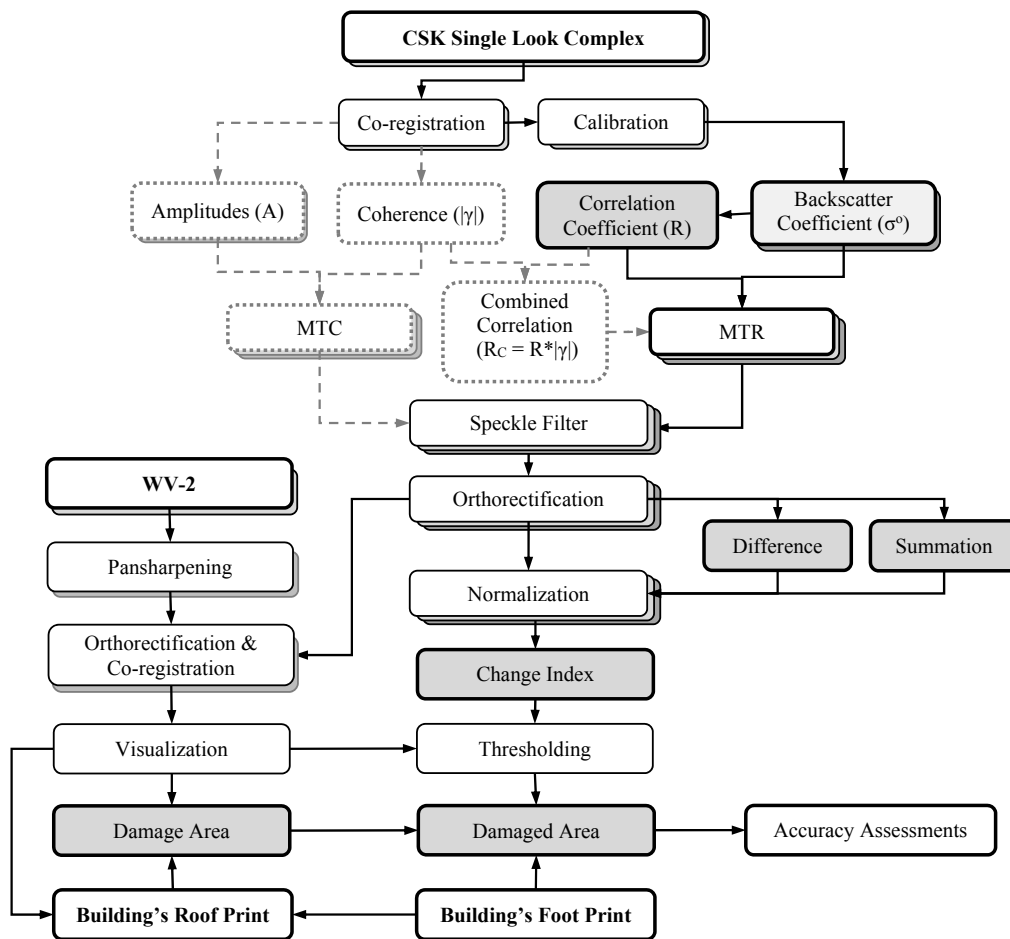


Fig. 2. Data flow diagram for Multitemporal Coherence (MTC) and Multitemporal Correlation (MTR) processing. Note that that the modules shown with dotted lines were not used to produce the final results.

(γ) and correlation coefficient (R) provide more information on the earth surface conditions, which vary within a small local area. However, using these measured values alone limits the interpretation because they do not indicate the trend of stage changes, which may be increasing or decreasing. Therefore, they are usually used in conjunction with a pair of amplitudes (intensity and backscatter coefficient) or their difference values. In various fields of change detection, RGB color composite mapping is considered to be a useful method [27, 28]. When a color composite is used, the results of the Multitemporal Coherence (MTC) and Multitemporal Correlation (MTR) methods can be represented by colors closer to natural ones, which are easier to understand [7, 8].

Because the coherence is a complex correlation coefficient, it is generally used as an absolute value or as the amplitude of coherence in real numbers. In a stable stage in which there is no change on the surface, the backscattering in the two images is equal. The coherence was high for the urban area, due to its high reflectivity and phase stability, but it was low for other land cover surfaces, because of the contribution of amplitudes and phase instability. Based on these results, white pixels were used to represent urban areas; yellow pixels were used to repre-

sent general land cover. Alternatively, the correlation coefficient had both positive and negative values, depending on the trend of the changes. Thus, in the stable stage, urban areas can have either white or yellow pixels, and general land cover is represented using light yellow pixels. In both cases, smooth surfaces, e.g., roads and bodies of water, may be either blue or black because of the ambiguity of the correlation. Lowcorrelation surfaces that have decreasing reflectances, e.g., areas that have flooded or that contain objects that have been removed from the scene, are shown in red, whereas those that have increasing reflectances, e.g., areas with destruction and that contain replaced objects in the scene, are shown in green.

To more clearly explain the color composition derived by the MTR method, an RGB color model is shown in **Fig. 4a**, and 3D scatter plots for each pixel are shown in **Figs. 4b-c** (displaying 1% of the pixels for rendering performance). The color gradient from black to blue represents smooth surfaces, such as bodies of water, roads, and runways, where the backscatter was low. Alternately, flooded areas that still remaining in the southern part of the city exhibit a reddish-magenta color due to the reduction of the backscatter. Other land cover and vegetation areas with low correlation coefficients can be recog-

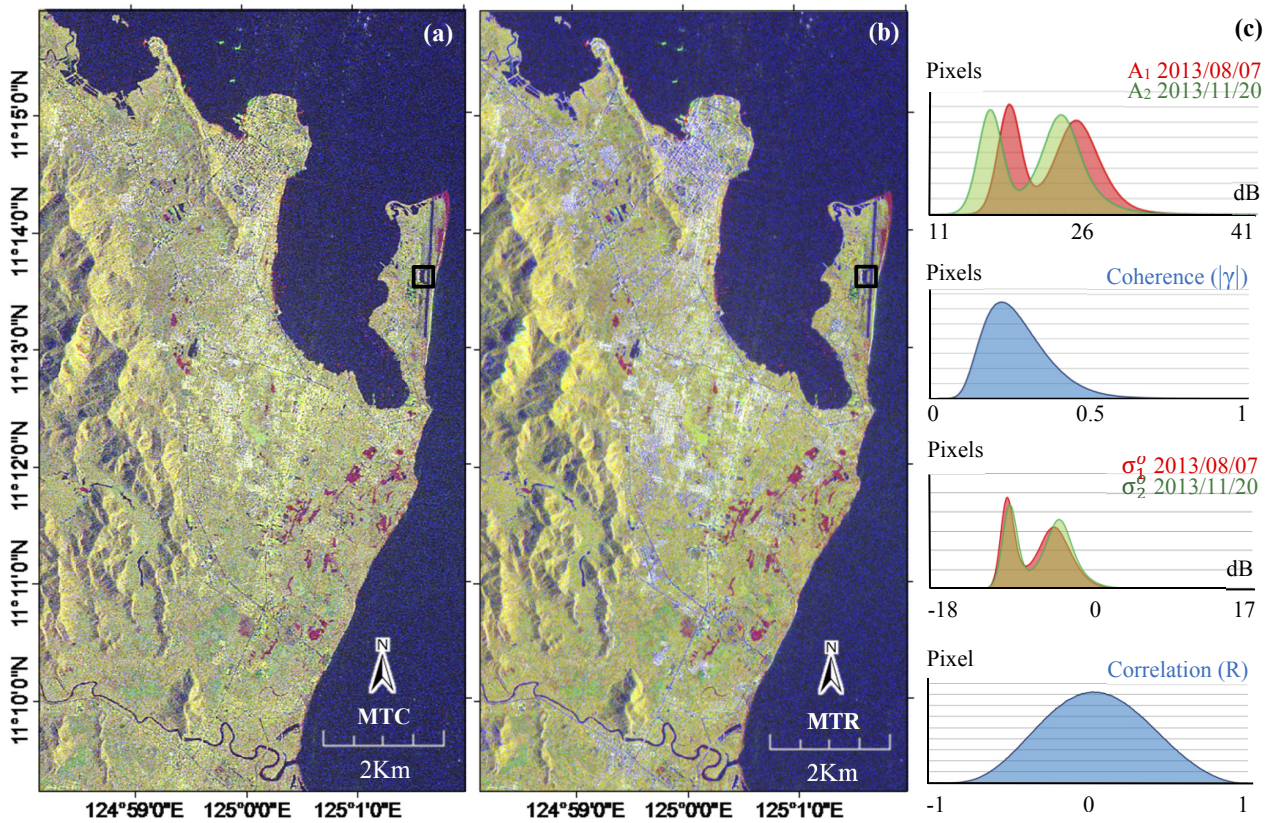


Fig. 3. (a) MTC and (b) MTR maps enhanced using the standard deviation technique and (c) their histograms.

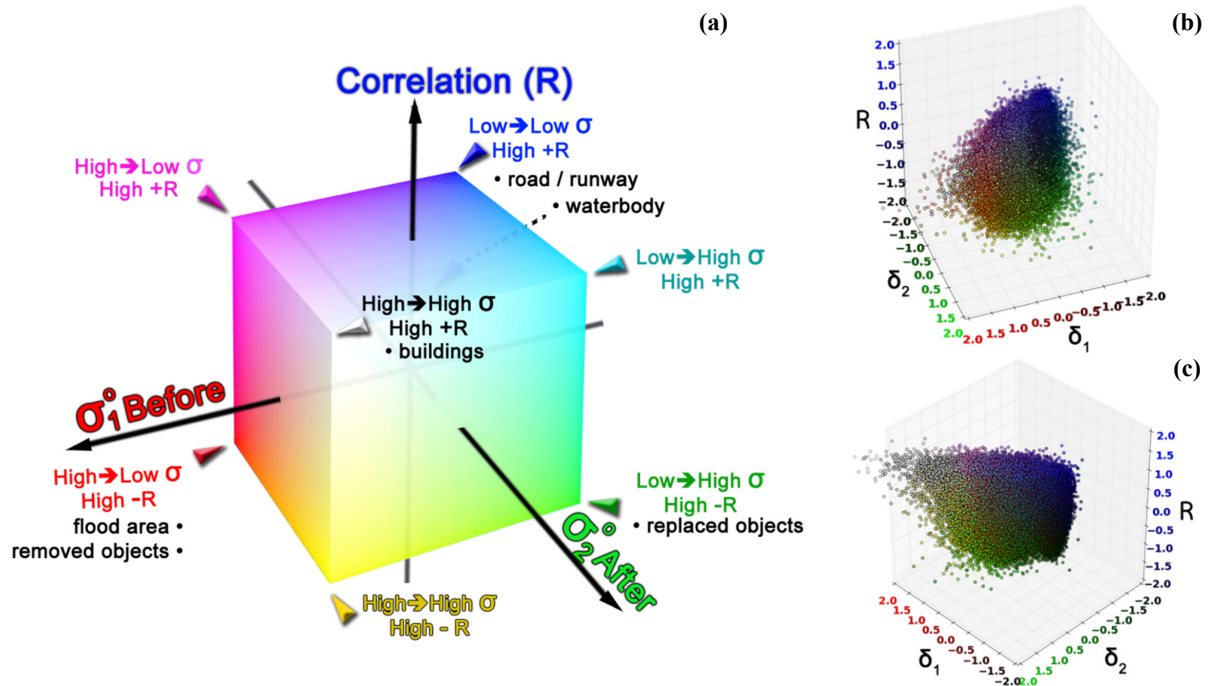


Fig. 4. (a) MTR demonstrated in the RGB color space. (b-c) 3D scatter plots of the MTR scaled by 2 times the standard deviation (2 SDs).

nized in yellow. The most important parts are the built-up areas in the city. If a building did not suffer damage, it is shown in white or yellow because its backscatter remained high with only slight changes. In contrast,

if the typhoon caused damage to a building, a decrease or increase in the backscatter can be observed. Due to the washing away of buildings/houses or the accumulation of debris, the MTR color composite is red (decreas-

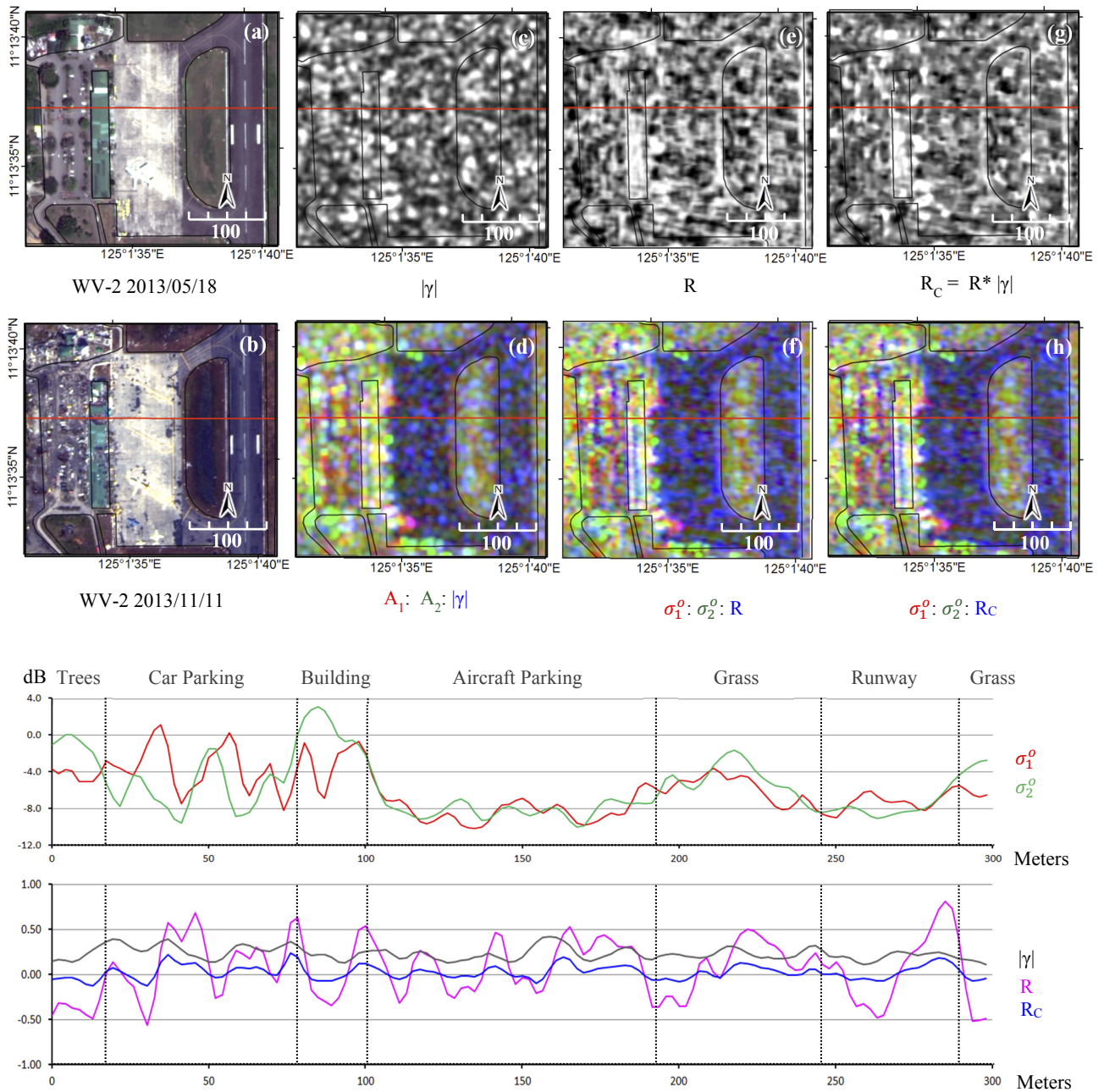


Fig. 5. Enlarged image of the Tacloban airport terminal: (a) WV-2 pre-event, (b) WV-2 post-event, (c) $|\gamma|$, (d) MTC, (e) R, (f) MTR, (g) RC and (h) MTRC maps, enhanced using the standard deviation technique.

ing backscatter with a high negative correlation), magenta (increasing backscatter with a high positive correlation), green (increasing backscatter with a high negative correlation) or cyan (increasing backscatter with a high positive correlation).

In this study, we attempted to use the correlation coefficient for several reasons. For example, the correlation coefficient can be applied to images that have lost their phase properties, e.g., multilook, calibrated and georeferenced data [29, 30], and the correlation coefficient can be calculated rapidly using real-valued operations. It can also be used in cases of decorrelation due to large perpendicular baselines. Another main reason that we chose the correlation coefficient is that it shows a two-tailed normal

distribution. This characteristic is suitable for our proposed method, which classifies the level of change from both sides of their mean. Since the coherence shows a one-tailed distribution, higher values refer to larger displacements, so it was inapplicable to the normalized value discussed in the next section. It might be used in different ways.

In the recent studies previously mentioned, several techniques have been attempted to combine the two statistics in order to retain the information contained in both and to improve overall accuracy. For example, the correlation coefficient has been used as the primary main statistic with the coherence used as a multiplier. As with the correlation coefficient, their product ranges from -1 to 1 .

We found that this combination did not greatly improve the results, and there was slightly more noise. Therefore, only the correlation coefficient was used for the processing in this study. Enlarged images of the Tacloban airport terminal and graphs of the corresponding profiles are shown in Fig. 5.

From the graphs of the profiles, the land cover was divided into 6 categories: trees, car parking areas, buildings, aircraft parking areas, grass, and runways. First, the aircraft parking areas and runways had the lowest reflectance. Some noise, the results of normal SAR characteristics and debris spread over the surfaces, was present. In contrast, the aircraft parking area and runway coherence was highest, although it was less than 0.5, and the correlation fluctuated between -0.5 and 0.5 . Second, the grass area had a higher reflectance and slightly lower coherence, and the correlation was distributed over a wider range. Third, the tree areas had increased reflectances, and the correlation coefficient was slightly more negative. This area could not be captured by the coherence because all trees were totally destroyed but median strips still remain. Next, the car parking area, which was a mix of empty space and three rows of trees, had combined characteristics and three peaks. Its reflectance decreased by an equivalent amount. Lastly, the east side of the Tacloban airport terminal building was destroyed, as evidenced by the area with the highest reflectance and reduced peak. The coherence slightly dropped in the damaged area, whereas the correlation coefficient was slightly negative.

4. Change Index

In the case of the visual interpretation, color composites produced by the MTC and MTR methods have slightly different representative colors, especially when normalized by the standard deviation. These maps provide more potential change information than two-color composites of the backscattering intensity (or coefficient) and are easier to visually interpret, but the process of using them to estimate damage is still complicated. Recent studies have used several change indices, including the difference, coherence and correlation coefficient, to detect and classify damage levels [7, 13, 31–33]. According to the color composite, red, green, cyan and magenta refer to pixels that have explicitly changed. Classifying them using a 2D model usually has some weaknesses, which will be discussed later. The new method in 3D space, the method proposed in this study, is expected to overcome shortcomings in the use of the change indices.

4.1. Difference and Summation

The difference (D) is a very simple index and is commonly used to indicate differences in spatial analyses, but the summation (S) has rarely been used. Both are calculated using the average value in a moving window. The two indices have a reciprocal relationship when expressed

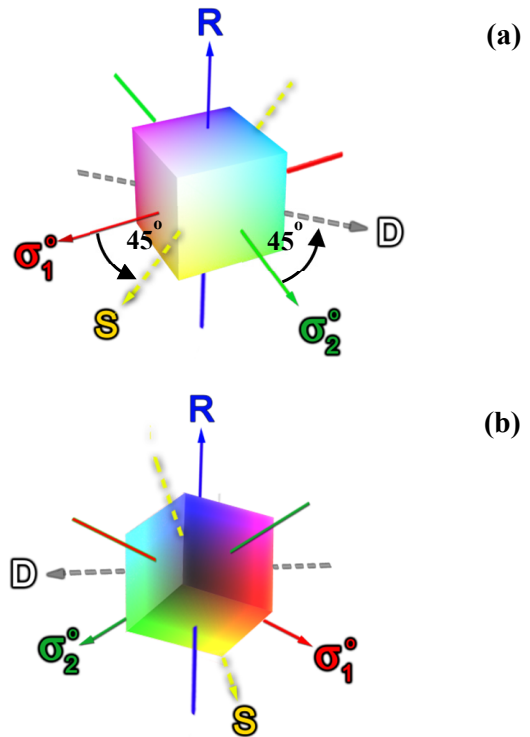


Fig. 6. (a) The rotation of the σ_1 and σ_2 axes 45° counterclockwise results in the Summation (S) and Difference (D) axes. (b) The backside view of (a).

in Euclidean vectors or a Cartesian coordinate system. When simultaneously rotating the pre-event values (σ_1^o to the red axis) and post-event values (σ_2^o to the green axis) 45° counterclockwise, the operation produces the subtraction (d) axis in Eq. (3) and the addition (s) axis in Eq. (4). In this case, the difference (D) and summation (S) can be obtained by multiplying d and s by a constant value, $\sqrt{2}$, as shown in Eq. (5). We can infer that the summation (S) is a value on the yellow axis and that the difference (D) is a value on the axis perpendicular to the S -axis in the red-green plane, as shown in Fig. 6. From this insight, the axis rotation, any equations composed of these parameters can be expressed in a 3D space.

$$d = \bar{\sigma}_2^o \cos 45^\circ - \bar{\sigma}_1^o \sin 45^\circ = \frac{\bar{\sigma}_2^o - \bar{\sigma}_1^o}{\sqrt{2}} \quad \dots \quad (3)$$

$$s = \bar{\sigma}_2^o \sin 45^\circ + \bar{\sigma}_1^o \cos 45^\circ = \frac{\bar{\sigma}_2^o + \bar{\sigma}_1^o}{\sqrt{2}} \quad \dots \quad (4)$$

$$D = \bar{\sigma}_2^o - \bar{\sigma}_1^o = \sqrt{2}d; \quad S = \bar{\sigma}_2^o + \bar{\sigma}_1^o = \sqrt{2}s \quad \dots \quad (5)$$

4.2. Change Index

Because the units and ranges of R , D , and S are not the same, a normalization was introduced. All of the factors used to calculate the change indices in this study were normalized by Eq. (6). Each pixel value was subtracted by the mean value and divided by twice the standard deviation (SD) of the entire image. Thus, a normalized positive value represents a value above the mean, a negative value represents a value below the mean, and 1.0 repre-

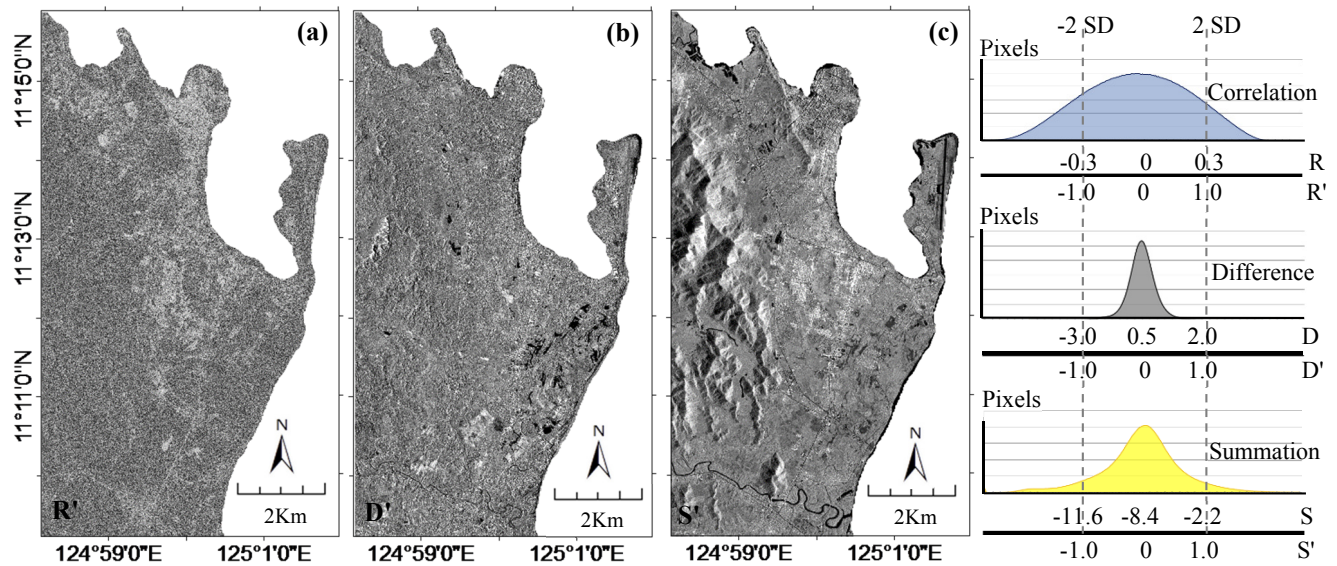


Fig. 7. (a) Normalized Correlation (R'), (b) Difference (D') and (c) Summation (S') obtained from the backscattering coefficients of the MTR map.

sents a value twice that of the standard deviation. Each normalized value (Z-score) is denoted using the prime symbol. According to the statistical three-sigma or 68–95–99.7 rule, which separates the normal distribution into three ranges using the standard deviation, normalized values of 1.0, which are located in range number 2, should cover 95% of the total pixels. Using the normalized score, it can be seen that D' is equivalent to d' and S' to s' in Eq. (6). The normalized results are shown in **Fig. 7**.

$$R' = \frac{R - \bar{R}}{2R_{SD}}; d' = D' = \frac{D - \bar{D}}{2D_{SD}}; s' = S' = \frac{S - \bar{S}}{2S_{SD}} \quad (6)$$

In this study, the absolute difference method (Δd) of Eq. (7) would give an ambiguous result because it could not discriminate between the blue and black pixels representing bodies of water and the white and the white and yellow pixels representing natural vegetation and buildings, according to the transformed RGB model shown in **Fig. 6**. Employing a combination using the correlation coefficient, as is used in some methods, would not improve the discrimination. For example, the weight method (Δw) [13] and the cylindrical or radius method (Δr) of Eq. (7) also have the same weaknesses.

$$\Delta d = |D'|; \Delta w = |D'| - 0.5R'; \Delta r = \sqrt{R'^2 + D'^2} \quad (7)$$

This problem can be solved by expressing the MTR in 3D space. A new change index is proposed and calculated using the normalized values of the difference (D'), summation (S'), and correlation (R'). According to the previous discussion, the D' -, S' - and R' -axes are mutually orthogonal. A hyperboloid of revolution can be obtained by rotating a hyperbola around its semi-minor axis (S'). The standard hyperboloid form in Eq. (8) is reduced to that in Eq. (9) when the constants a , b , and c are equal to 1. When a , b , and c are not equal to 1, a standard deviation weight instead of the 2 in Eq. (6) can be introduced

to simplify the hyperboloid equation.

$$H' = \frac{R'^2}{a^2} + \frac{D'^2}{b^2} - \frac{S'^2}{c^2} \dots \dots \dots (8)$$

$$H' = R'^2 + D'^2 - S'^2; \text{ when } a = b = c = 1 \dots \dots (9)$$

All of the R' , D' , and S' values that return the same H' value in the equation are located on the same hyperboloid surface. Negative values representing a hyperboloid of two sheets indicate a greater similarity. Zero values represent a conical surface, the differences and similarities of which are almost equal. Positive values representing a hyperboloid of one sheet indicate greater differences. By spreading the hyperboloid “spittoon,” as shown in **Fig. 8d**, this operation was capable of differentiating among bodies of water, natural vegetation and buildings. Because the H' value is calculated using the quadratic polynomial formula, each range on the scale is squared. The change index value is much easier to recognize in the linear scale if the square root is taken. Because H' can be a positive or negative number, the square root must apply to the absolute value of H' , and its sign must be retained, as in the definition of the Hyperboloid Change Index (Δh) in Eq. (10).

$$\Delta h = \text{sign}(H') \sqrt{|H'|} \dots \dots \dots (10)$$

A comparison of the results obtained using the proposed method and those obtained using other candidate methods is shown in **Fig. 8**. Among those methods, Δh demonstrated the best classification capability. This is mainly because it was developed from three parameters, which included the summation in the equation in such a way that the magnitude of the intensity from the original data is preserved. This index can indicate the change in conjunction with the reflectance, so its appearance is much clearer than those of the other indices. It is capable

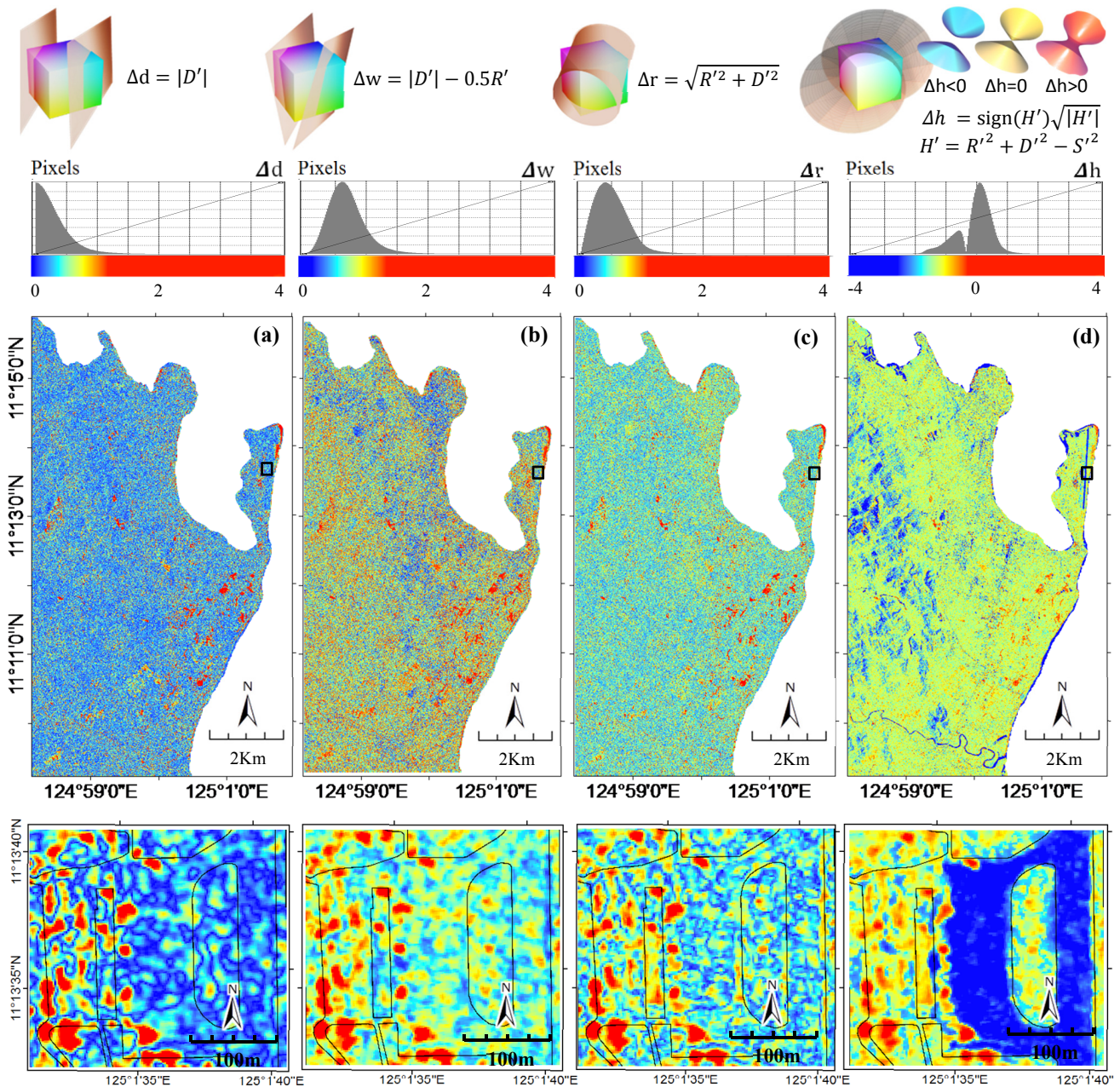


Fig. 8. Results of the change detection using the candidate methods: (a) absolute difference (Δd), (b) weight (Δw), (c) circular (Δr), (d) proposed hyperboloid method (Δh) and enlarged images of the Tacloban airport terminal.

of distinguishing changes very clearly. Moreover, the difference between the sea and mainland can easily be identified. Yellow areas with slightly positive values represent slight changes, such as the changes seen in the natural vegetation. Blue areas with high negative values were almost unchanged over the period. These included bodies of the water, roads, runways and buildings. In this case, a double bounce effect area can be identified as corresponding to a very low value of the index, since the summation of the intensity is very high, as in the case of the deep blue on the eastern side of the Tacloban airport terminal buildings, for instance. Although Δh was able to capture this phenomenon, which could not have been captured by the other indices, the area was not identified as an area of de-

struction, because the reflection from building walls was hard to see in nadir images acquired from optical satellites. Red areas with highly positive values represent significant changes, such as damaged and flooded areas or the growth of agricultural plants. For large buildings, the index value was high due to the loss of surface. Therefore, the reflectance was increased, with a high correlation. The growth of vegetation over a period of 105 days, as shown on the map, would not be counted as damage caused by the typhoon. To avoid this possibility, the pair of SAR images should be taken over the shortest possible time interval.

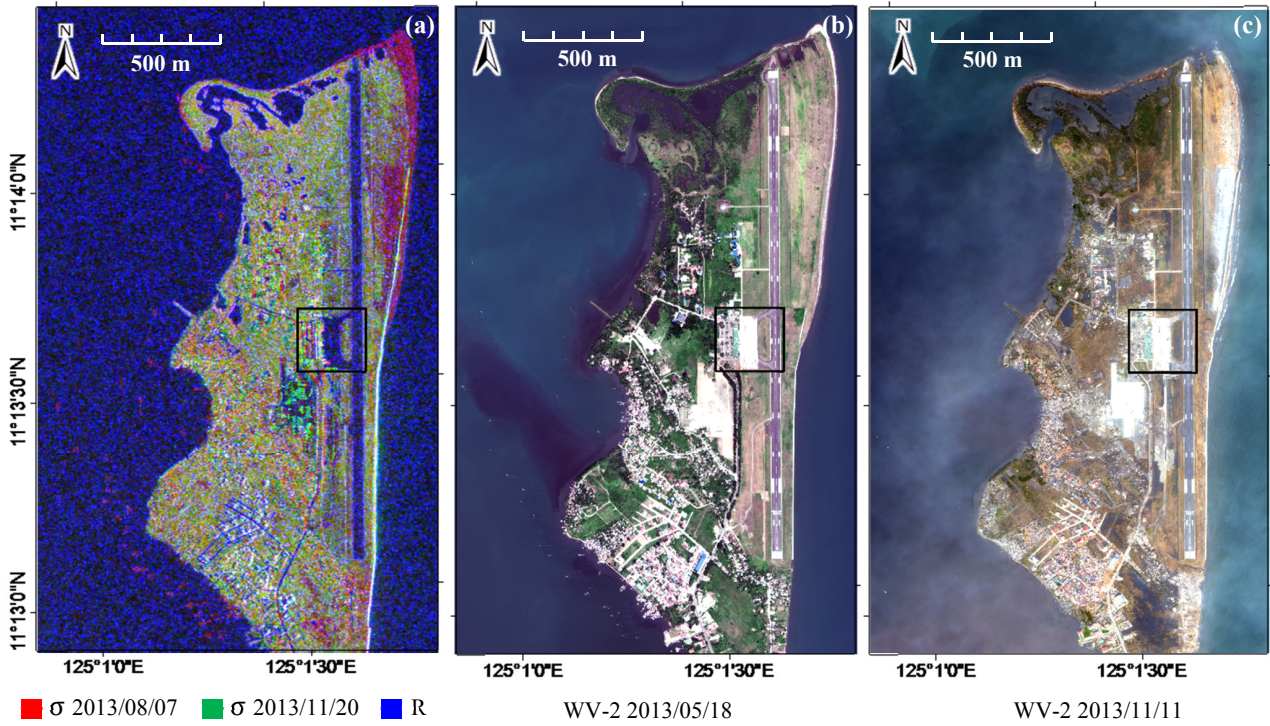


Fig. 9. Enlarged images of the Tacloban airport: (a) MTR map, (b) the pre-event WV-2 image and (c) the post-event WV-2 image. Black-bordered areas are close-ups of Tacloban airport.

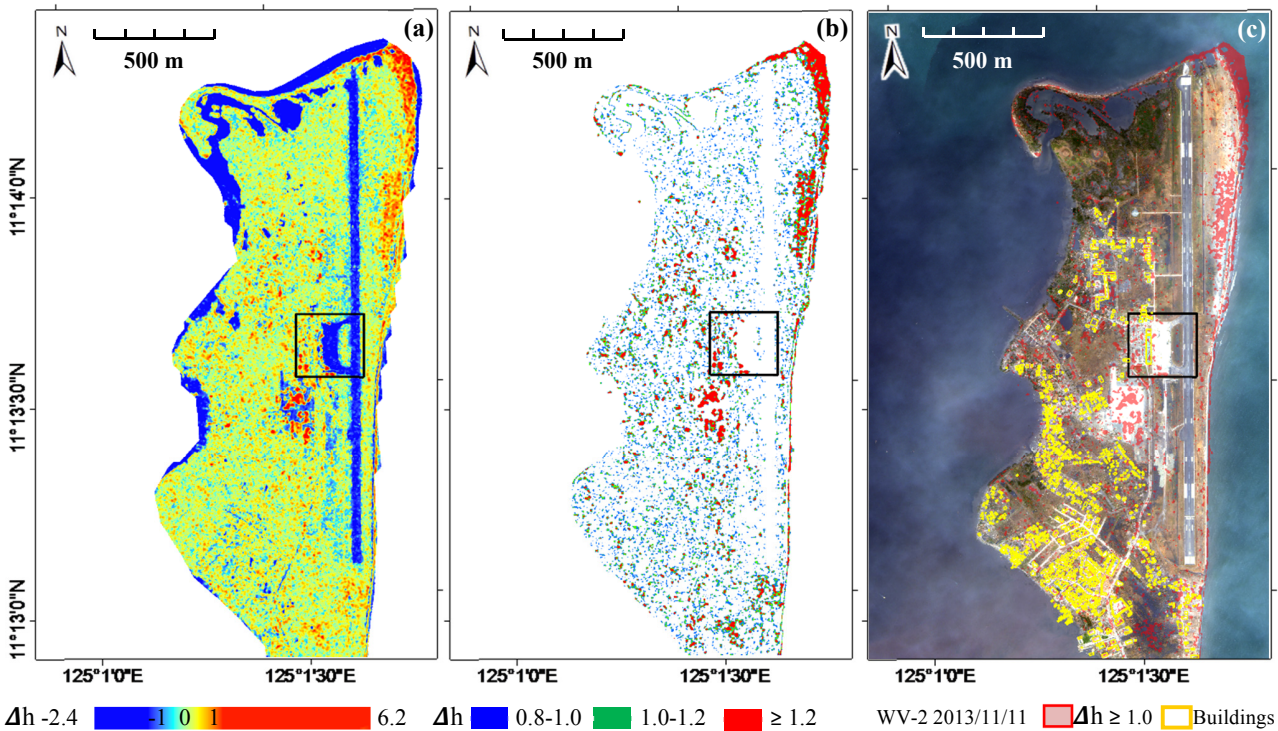


Fig. 10. Assessment of damage to Tacloban airport: (a) Hyperboloid Change Index (Δh), (b) thresholding into 3 classes, (c) the extracted damage areas overlapping on the post-event WV-2 image. Black-bordered areas are close-ups of Tacloban airport.

5. Damage Extraction and Accuracy Evaluation

Thresholding is the simplest method of evaluating damage levels. A suitable threshold value for the Hyperboloid Change Index (Δh) was selected by comparing its results

with the high-resolution optical images. Because of limitations in visibility due to cloud cover, two WV-2 images taken 177 days apart were selected and used as the truth data. An enlargement of a sample area at the Tacloban airport is shown in **Fig. 9**. Because the changed index value was designed to be a function of the standard de-

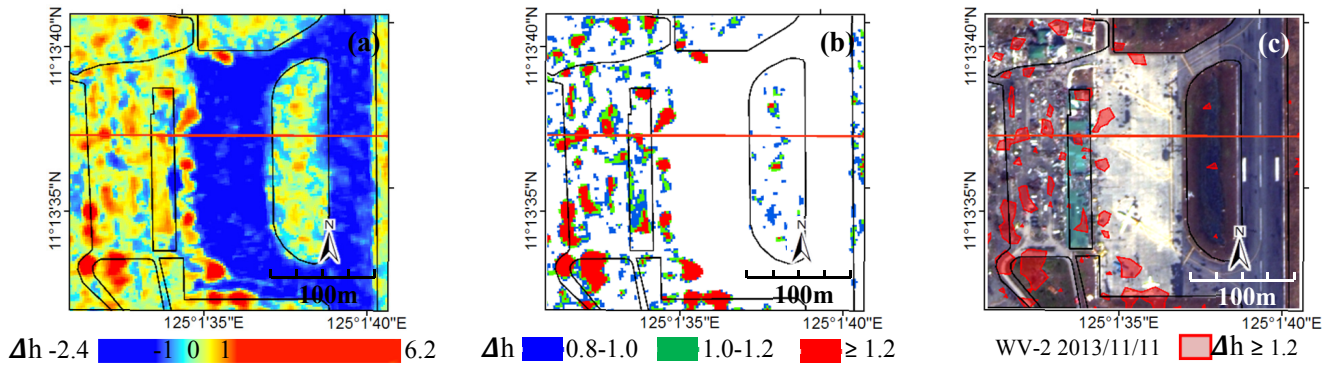


Fig. 11. Assessment of damage to Tacloban airport: (a) Hyperboloid Change Index (Δh), (b) thresholding into 3 classes, and (c) the extracted damage areas superimposed on the post-event WV-2 image.

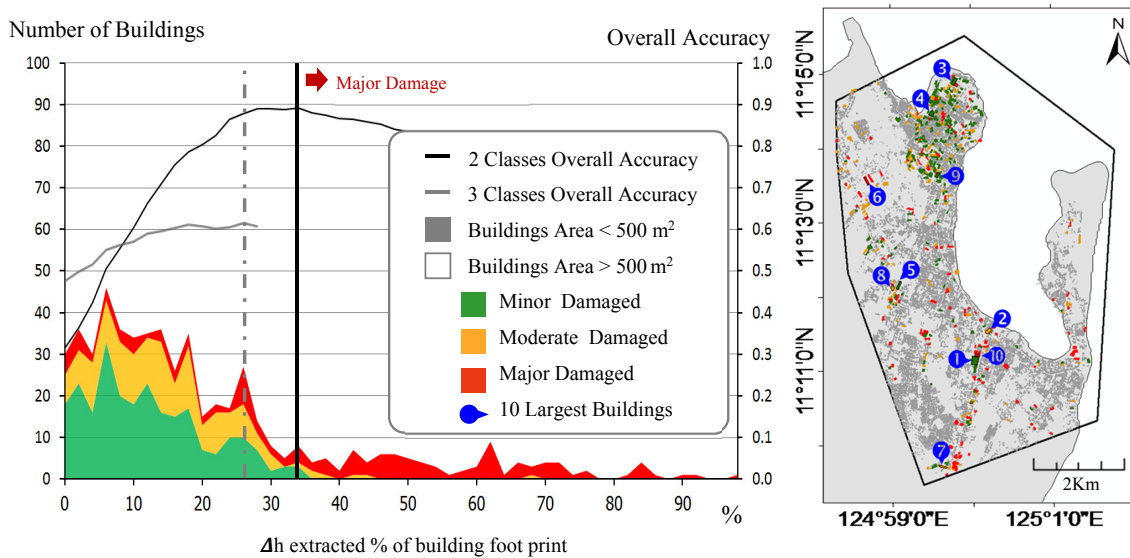


Fig. 12. Damage extraction diagram when Δh 's threshold 1.2 for 545 large buildings with footprint areas is more than 500 m², shown in the right-side map. The damage levels were classified to 3 classes by visual inspection of the WV-2 images.

viation, a value of 1.0 is equivalent to twice the standard deviation, which covers approximately 95% of the total pixels. Therefore, the threshold value would be close to 1.0. By varying the threshold by trial-and-error to suitably detect damage with the least noise, a value of 1.0 was selected. The extraction result is shown in **Fig. 10b**, wherein the image has been classified into 3 classes. The classes with threshold values lower than 1.0 appear noisy. Enlarged images of the Tacloban airport terminal are shown in **Fig. 11**.

The coastal erosion of the northeastern cape can be easily distinguished from the WV-2 image and the extracted results from the proposed method. Moreover, destruction offshore, e.g., fish traps and boats, can also be observed along the west coast in **Figs. 9** and **10**.

For the building damage detection, the results obtained using the same threshold value sufficiently revealed the damage. It was difficult to separate the buildings from much of the debris spread throughout the city, and the resolution of the CSK images made accurate assessment difficult. Building damage detection from remote sensing

imagery can be carried out by several sensors, e.g. optical, SAR, and LiDAR. In this regard, the optical imagery with spatial resolution finer than one meter is well suited to be a reference data source. Because optical satellite images are acquired with views almost from the nadir, only building information on roof and the presence/absence of debris around the lateral walls are collected [34]. Although the superimposition of pre- and post-event optical images results in automated change detection, visual interpretation is widely used in practice [35]. Based on a field survey and a visual interpretation of high-resolution optical satellite images, the damage level, focusing on the roofs, was classified into two categories by Tohoku University [36]. The high damage or destruction class was used when the roof of a building had been reduced by more than 50% or the structure had been washed or blown away. The low damage or survival class was used for buildings with small variations in their geometry or roof shape. Unlike optical sensors, a SAR sensor can capture, due to its oblique observation scheme, more information relevant to lateral wall damage, but its performance in urban areas is

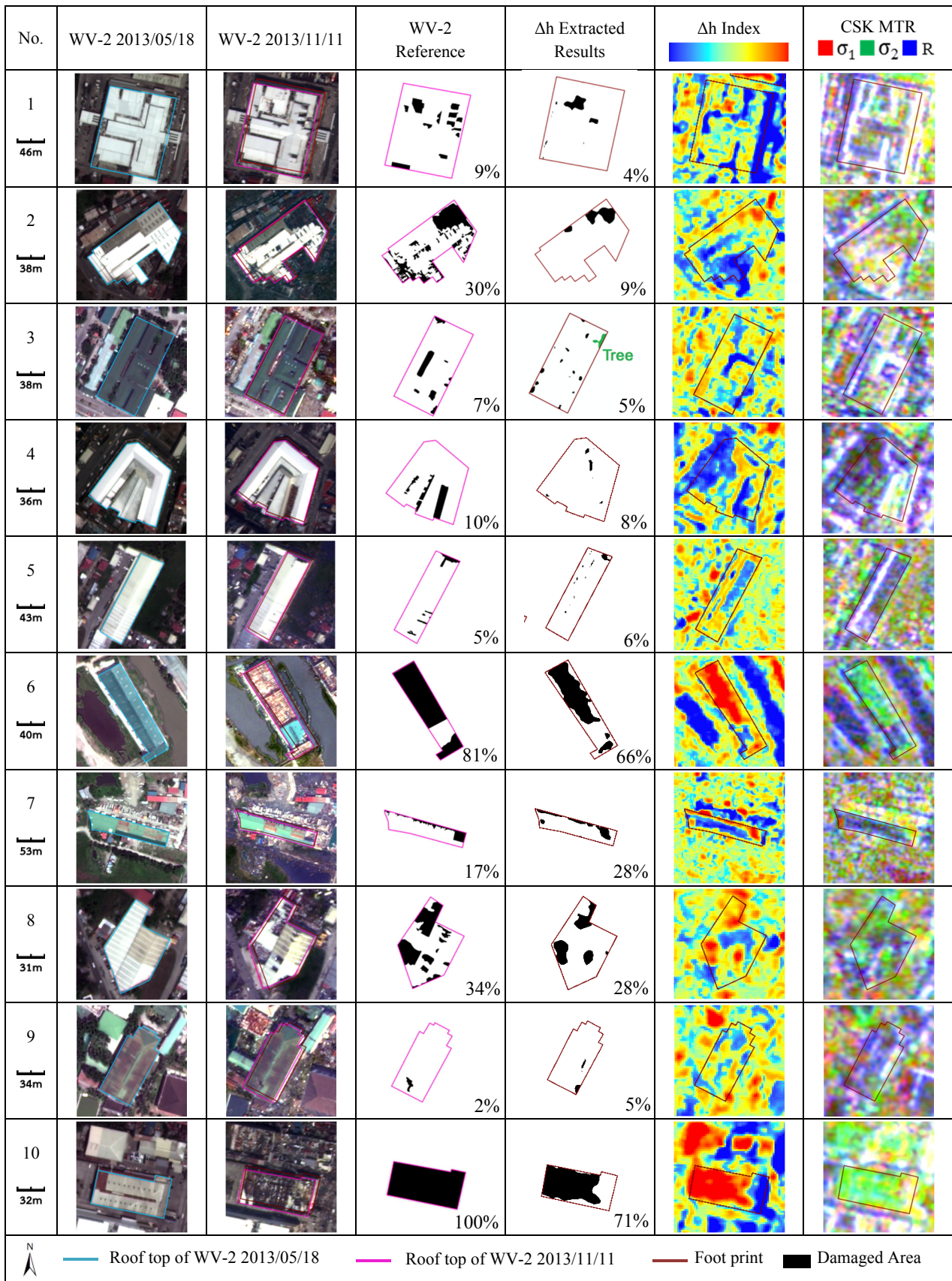


Fig. 13. Comparison of the results obtained using the proposed damage extraction method and the reference damage areas from the WV-2 images for the 10 largest buildings.

Table 2. Comparison of candidate methods to Δh by extracted area, best accuracy, and percent of footprint.

| Method | Threshold = 1.0 | | | | Extracted Area = 3.72% | | | |
|------------|-----------------|-----------------------|---------------|-------------------|------------------------|-----------------------|---------------|-------------------|
| | Extracted Area | Overlap to Δh | Best Accuracy | At % of footprint | Threshold | Overlap to Δh | Best Accuracy | At % of footprint |
| Δd | 5.19% | 80% | 89% | 24% | 1.11 | 71% | 89% | 20% |
| Δw | 7.57% | 80% | 89% | 26% | 1.23 | 71% | 89% | 16% |
| Δr | 12.65% | 100% | 83% | 40% | 1.28 | 83% | 89% | 22% |
| Δh | 3.72% | 100% | 89% | 32% | 1.00 | 100% | 89% | 32% |

Table 3. Confusion matrix of Δh for the 2-class damage extraction from the CSM images.

| | | Visual inspection of WV-2 images | | | |
|------------------------------------|--------------------|----------------------------------|-------|-------|---------------|
| | | Minor & Moderate | Major | Total | User Accuracy |
| Δh from CSM | Minor & Moderate | 393 | 48 | 441 | 0.89 |
| | Major | 12 | 92 | 104 | 0.88 |
| | Total | 405 | 140 | 545 | |
| | Procedure Accuracy | 0.97 | 0.66 | | 0.89 |
| Cohen's kappa for 2 Classes = 0.69 | | | | | |

Table 4. Confusion matrix of Δh for the 3-class damage extraction from the CSM images.

| | | Visual inspection of WV-2 images | | | | |
|------------------------------------|--------------------|----------------------------------|----------|-------|-------|---------------|
| | | Minor | Moderate | Major | Total | User Accuracy |
| Δh from CSM | Minor | 236 | 144 | 41 | 421 | 0.56 |
| | Moderate | 6 | 7 | 7 | 20 | 0.35 |
| | Major | 5 | 7 | 92 | 104 | 0.88 |
| | Total | 247 | 158 | 140 | 545 | |
| | Procedure Accuracy | 0.96 | 0.04 | 0.66 | | 0.61 |
| Cohen's kappa for 3 Classes = 0.35 | | | | | | |

limited by shadowing and layover issues [37].

Due to the lateral observations and surface roughness measurements inherent to SAR, the backscatter from a cluster of small buildings when they were destroyed would be reduced because of the reduction of the double bounce effect. Furthermore, this effect can strongly reduce backscatter when numerous buildings are washed away [38].

In this study, the extracted results had low accuracy for small buildings in dense areas, but accuracy was good enough to extract the damaged portions of large buildings. The damage assessment was examined using 545 large buildings with footprint areas larger than 500 m², buildings that were selected from auxiliary vector data. The damage was visually assessed from roofs in the pre- and post-event WV-2 images. The damage was then assigned to three classes using the relative damaged area in the footprint of each building: less than 10% as no damage or minor damage, from 10% to 50% as moderate damage, and more than 50% as major damage or collapse. The statistical results are plotted in Fig. 12, and enlarged images for the 10 largest buildings are shown in Fig. 13.

The classification procedure was carried out in two steps. First, the major damage was classified. The moderate damage was then distinguished from the minor damage. The threshold value was selected by the extracted % of building footprint that returned the best accuracy.

Comparison results in Table 2 show that the proposed index Δh was better than that of other candidate methods. Although all methods yielded good accuracy with almost the same value, 89%, the proposed index result was superior in terms of damage extraction for several reasons. First, it had the lowest amount of noise in the extracted area. Second, it captured the damage to buildings with the best performance, as the damage level extracted from the area was highest with the proposed method, close to 50%, which we define as major damage.

In the case of Δh , the major damage class (32%) was identified with relatively good accuracy (user accuracy of 0.88, producer accuracy of 0.66) from the extracted results. At this point, a maximum overall accuracy of 0.89 and Cohen's kappa of 0.69 was returned in the confusion matrix shown in Table 3. It is also notable that the minor damage could not be distinguished from the moderate damage in the extracted results. In the case of separating moderate damage from minor damage with the criterion of 28%, the overall accuracy dropped to 0.61 and the Cohen's kappa to 0.35 in the confusion matrix shown in Table 4. Because the moderate damage class was proportionally lower than the others, with any percentage of roof damage being classified as moderate, we were unable to correctly extract the moderate damage class from the minor damage class. Therefore, the damage levels were grouped into only two classes by combining the minor and

moderate damage classes.

In total, 140 buildings were classified as having sustained major damage. By using the proposed method, 104 buildings were extracted, and from those, the classification of 92 buildings (66%) was correctly estimated. There were 405 buildings in the minor-to-moderate damages class, and a total of 441 buildings were extracted, with 393 buildings (97%) correctly classified. Note that the damaged areas of the buildings detected using this method relied on the SAR and auxiliary vector data and that some pixels around the selected buildings were assigned to the damaged area. Some of those pixels were the damaged areas of other buildings and were not included in this study. However, some of the pixels were affected by changes in the environment, including flooded areas, broken trees and debris. Those pixels should be classified as false alarms.

6. Conclusions

The devastation wrought by the 2013 typhoon Haiyan was investigated using a Multi-temporal Correlation (MTR) technique applied to two CSK images. A new change index was introduced, and of the several candidate methods, the proposed Hyperboloid Change Index (Δh) method, achieved the greatest building damage extraction accuracy (89%) when distinguishing moderate damage from minor damage. The proposed index was able to indicate, with lower noise, changes over a period. Its value was normalized and related to the standard deviation of the difference and the correlation between the pre- and post-event backscattering coefficients. For this event, the index was able to efficiently extract, given a proper threshold value, the severe damage to fish traps and large buildings. However, some limitations were observed, including an inability to handle small buildings and/or dense areas as well as relatively poor accuracy in distinguishing minor to moderate damage levels for large buildings. These limitations of the proposed technique are probably related to the spatial resolution and SAR observation scheme, so they cannot be avoided.

The proposed Hyperboloid Change Index has clear advantages with respect to other candidate methods because it can indicate a change in conjunction with the reflectance. The resulting change maps are clearer and easier to interpret than the maps produced using the other tested indices. The method is not only suitable for detecting damage to buildings, but it can also be used generally to differentiate levels of change. It is possible that further improvements can be made by adjusting the hyperboloid constants or the standard deviation coefficients, according to the specific case. This improvement, in addition to testing the influence of the window size, will be among the main issues considered in future research.

Acknowledgements

We would like to extend our appreciation to Dr. Marc Wieland for his comments and assistance with the technical writing in this article. This study was supported financially by a grant-in-aid for Scientific Research (project numbers 24241059 and 26882009).

References:

- [1] F. Adragna and J. Nicolas, "Interferometry. In Processing of Synthetic Aperture Radar Images," H. Maitre (Ed.), John Wiley & Sons, ISTE Ltd, London, UK, pp. 279-300, 2008.
- [2] M. E. Engdahl and J. M. Hyypa, "Land-Cover Classification Using Multitemporal ERS-1/2 InSAR Data," *IEEE Trans. Geosci. Remote Sens.*, Vol.41, 2003.
- [3] L. Bruzzone and A. Wiesmann, "An Advanced System for the Automatic Classification of Multitemporal SAR Images," *IEEE Trans. Geosci. Remote Sens.*, Vol.42, pp. 1321-1333, 2004.
- [4] L. Xu, S. Li, Y. Deng, and R. Wang, "Unsupervised classification of polarimetric synthetic aperture radar interferometry using polarimetric interferometric similarity parameters and SPAN," *IET Radar Sonar Navig.*, Vol.8, pp. 1135-1144, 2014.
- [5] P. Mishra and D. Singh, "A Statistical-Measure-Based Adaptive Land Cover Classification Algorithm by Efficient Utilization of Polarimetric SAR Observables," *IEEE Trans. Geosci. Remote Sens.*, Vol.52, pp. 2889-2900, 2014.
- [6] J. G. Liu, A. Black, H. Lee, H. Hanaizumi, and J. Moore, "Land surface change detection in a desert area in Algeria using multi-temporal ERS SAR coherence images," *Int. J. of Remote Sensing*, Vol.22, pp. 2463-2477, 2001.
- [7] A. Refice, D. Capolongo, G. Pasquariello, A. D'Addabbo, F. Bovenga, R. Nutricato, F. P. Lovergine, and L. Pietranera, "SAR and InSAR for Flood Monitoring: Examples With COSMO-SkyMed Data," *IEEE J. Sel. Top. Appl. Earth Obs. Remote Sens.*, Vol.6, pp. 2711-2722, 2014.
- [8] D. Amitrano, G. Di Martino, A. Iodice, D. Riccio, and G. Ruello, "A New Framework for SAR Multitemporal Data RGB Representation: Rationale and Products," *IEEE Trans. Geosci. Remote Sens.*, Vol.1, pp. 117-133, 2015.
- [9] M. Preiss, D. A. Gray, and N. J. S. Stacy, "Detecting Scene Changes Using Synthetic Aperture Radar Interferometry," *IEEE Trans. Geosci. Remote Sens.*, Vol.44, pp. 2041-2054, 2006.
- [10] B. Xiong, J.M. Chen, and G. Kuang, "A change detection measure based on a likelihood ratio and statistical properties of SAR intensity images," *Remote Sensing Letters*, Vol.3, pp. 267-275, 2012.
- [11] A. Bouaraba, A. Younsi, A. Belhadj-Aissa, M. Acheroy, N. Milisavljevic, and D. Closson, "Robust Techniques For Coherent Change Detection Using Cosmo-SkyMed Sar Images," *Progress In Electromagnetics Research M*, Vol.22, pp. 219-232, 2012.
- [12] E. J. M. Rignot and J. van Zyl, "Change Detection Techniques for ERS-1 SAR Data," *IEEE Trans. Geosci. Remote Sens.*, Vol.31, pp. 896-906, 1993.
- [13] W. Liu, F. Yamazaki, H. Gokon, and S. Koshimura, "Extraction of Tsunami-Flooded Areas and Damaged Buildings in the 2011 Tohoku-Oki Earthquake from TerraSAR-X Intensity Images," *Earthquake Spectra*, Vol.29, S1, pp. S183-S200, 2013.
- [14] S. Stramondo, C. Bignami, M. Chini, N. Pierdicca, and A. Terzilliani, "Satellite radar and optical remote sensing for earthquake damage detection: Results from different case studies," *Int. J. Remote Sens.*, Vol.27, pp. 4433-4447, 2006.
- [15] C. Yonezawa and S. Takeuchi, "Decorrelation of SAR data by urban damages caused by the 1995 Hyogoken-nanbu earthquake," *Int. J. Remote Sens.*, Vol.22, pp. 1585-1600, 2001.
- [16] S. Takeuchi, Y. Suga, C. Yonezawa, and A. J. Chen, "Detection of Urban Disaster Using InSAR – A Case Study for the 1999 Great Taiwan Earthquake," *In Proc. of the IEEE IGARSS, Honolulu, HI, USA*, 24–28 July, pp. 339-341, 2000.
- [17] Y. Suga, S. Takeuchi, Y. Oguro, A.J. Chen, M. Ogawa, T. Konishi, and C. Yonezawa, "Application of ERS-2/SAR data for the 1999 Taiwan earthquake," *Adv. Space Res.*, Vol.28, pp. 155-163, 2001.
- [18] M. Matsuoka and F. Yamazaki, "Characteristics of Satellite SAR Images in the Areas Damaged by Earthquakes," *In Proc. of the IEEE IGARSS, Honolulu, HI, USA*, 24–28 July 2000, pp. 2693-2696.
- [19] D. Brunner, G. Lemoine, and L. Bruzzone, "Earthquake Damage Assessment of Buildings Using VHR Optical and SAR Imagery," *IEEE Trans. Geosci. Remote Sens.*, Vol.48, pp. 2403-2419, 2010.
- [20] National Disaster Risk Reduction and Management Council, Republic of the Philippines, NDRRMC Update: Updates re Effects of Typhoon Yolanda (Haiyan), 17 April 2014, [http://www.ndrrmc.gov.ph/attachments/article/1329/Update_on_Effects_Typhoon_YOLANDA_\(Haiyan\)_17APR2014.pdf](http://www.ndrrmc.gov.ph/attachments/article/1329/Update_on_Effects_Typhoon_YOLANDA_(Haiyan)_17APR2014.pdf) [accessed Jun. 29, 2015]

- [21] A. M. F. Lagmay, R. P. Agaton, M. A. C. Bahala, J. B. L. T. Briones, K. M. C. Cabacaba, C. V. C. Caro, L. L. Dasallas, L. A. L. Gonzalo, C. N. Ladiero, J. P. Lapidez et al., "Devastating storm surges of Typhoon Haiyan," *Int. J. of Disaster Risk Reduction*, Vol.11, pp. 1-12, 2015.
- [22] F. Covello, F. Battaza, A. Coletta, E. Lopinto, C. Fiorentino, L. Pietranera, G. Valentini, and S. Zoffoli, "COSMO-SkyMed an existing opportunity for observing the Earth," *J. of Geodynamics*, Vol.49, pp. 171-180, 2010.
- [23] The Earth Observation and Geo-Spatial Information (e-GEOS). Cosmo-SkyMed Image Calibration, http://www.e-geos.it/products/pdf/COSMO-SkyMed-Image_Calibration.pdf [access Jun. 29, 2015]
- [24] S. Parrilli, M. Poderico, C.V. Angelino, and L. Verdoliva, "A Nonlocal SAR Image Denoising Algorithm Based on LLMSE Wavelet Shrinkage," *IEEE Trans. Geosci. Remote Sens.*, Vol.50, No.2, pp. 606-616, 2012.
- [25] M. Born and E. Wolf, "Principles of Optics: Electromagnetic Theory of Propagation, Interference and Diffraction of Light," 4th ed., Pergamon Press, London, England, pp. 191-554, 1970.
- [26] A. Ferretti, A. Monti-Guarnieri, C. Prati, and F. Rocca, "Part C InSAR processing: a mathematical approach," In "InSAR Principles: Guidelines for SAR Interferometry Proc. and Interpretation," K. Fletcher (Ed.), ESA Publications, Noordwijk, Netherlands, pp. 3-13, 2007.
- [27] F. Cigna, D. Tapete, R. Lasaponara, and N. Masini, "Amplitude change detection with Envisat ASAR to image the cultural landscape of the Nasca region, Peru," *Archaeol. Prospect.*, Vol.20, pp. 117-131, 2013.
- [28] D. Tapete, F. Cigna, N. Masini, and R. Lasaponara, "Prospection and Monitoring of the Archaeological Heritage of Nasca, Peru, with ENVISAT ASAR," *Archaeol. Prospect.*, Vol.20, pp. 133-147, 2013, doi: 10.1002/arp. 1449.
- [29] B. Aiazzi, L. Alparone, S. Baronti, and A. Garzelli, "Coherence Estimation From Multilook Incoherent SAR Imagery," *IEEE Trans. Geosci. Remote Sens.*, Vol.41, pp. 2531-2539, 2003.
- [30] Z. Chang, H. Gong, J. Zhang, and M. Chen, "Correlation Analysis on Interferometric Coherence Degree and Probability of Residue Occurrence in Interferogram," *IEEE Sensors J.*, Vol.14, pp. 2369-2375, 2014.
- [31] V. Onana, E. Trouvé, G. Mauris, J. Rudant, and E. Tonyé, "Linear Features Extraction in Rain Forest Context From Interferometric SAR Images by Fusion of Coherence and Amplitude Information," *IEEE Sensors J.*, Vol.41, pp. 2540-2556, 2003.
- [32] G. A. Arciniegas, W. Bijker, N. Kerle, and V. A. Tolpekin, "Coherence- and Amplitude-Based Analysis of Seismogenic Damage in Bam, Iran, Using ENVISAT ASAR Data," *IEEE Trans. Geosci. Remote Sens.*, Vol.45, pp. 1571-1581, 2014.
- [33] F.C. Conesa, N. Devanthery, A.L. Balbo, Marco. Madella, and O. Monserrat, "Use of Satellite SAR for Understanding Long-Term Human Occupation Dynamics in the Monsoonal Semi-Arid Plains of North Gujarat," *India. Remote Sens.*, Vol.6, No.11, pp. 11420-11443, 2014.
- [34] N. Kerle and R.R. Hoffman, "Collaborative damage mapping for emergency response: the role of Cognitive Systems Engineering," *Nat. Hazards Earth Syst. Sci.*, Vol.13, No.1, pp. 97-113, 2013.
- [35] L. G. Dong and J. Shan, "A comprehensive review of earthquake-induced building damage detection with remote sensing techniques," *ISPRS J. Photogramm. Remote Sens.*, Vol.84, pp. 85-99, 2013.
- [36] E. Mas, J. Bricker, S. Kure, B. Adriano, C. Yi, A. Suppasri, and S. Koshimura, "Field survey report and satellite image interpretation of the 2013 Super Typhoon Haiyan in the Philippines," *Nat. Hazards Earth Syst. Sci.*, Vol.15, pp. 805-816, 2012.
- [37] F. Dell'Acqua and P. Gamba, "Remote sensing and earthquake damage assessment: Experiences, limits, and perspectives," *Proc. of the IEEE.*, Vol.100, No.10, pp. 2876-2890, 2012.
- [38] M. Chini, A. Piscini, F. R. Cinti, S. Amici, R. Nappi, and P. M. de Martini, "The 2011 Tohoku (Japan) Tsunami inundation and liquefaction investigated through optical, thermal, and SAR data," *IEEE Geosci. Remote Sens. Lett.*, Vol.10, pp. 347-35, 2013.



Name:
Pisut Nakmuenwai

Affiliation:
Ph.D. Student, Graduate School of Engineering,
Chiba University

Address:
1-33 Yayoi-cho, Inage-ku, Chiba 263-8522, Japan

Brief Career:
2000-2003 Forest Technical Officer, Royal Forest Department, Bangkok, Thailand
2003-2005 Computer Scientist, Consultant of Technology Co. Ltd. Bangkok, Thailand
2005-2010 Computer Scientist, Geo-Informatics and Space Technology Development Agency, Bangkok, Thailand
2010- Senior Computer Scientist, Geo-Informatics and Space Technology Development Agency, Bangkok, Thailand
2012- Graduate Student, Chiba University

Academic Societies & Scientific Organizations:
• Remote Sensing and GIS Association of Thailand



Name:
Fumio Yamazaki

Affiliation:
Professor, Department of Urban Environment
Systems, Chiba University

Address:
1-33 Yayoi-cho, Inage-ku, Chiba 263-8522, Japan

Brief Career:
1978 Research Engineer, Shimizu Corporation, Japan
1989 Associate Professor, Institute of Industrial Science, University of Tokyo
2001 Professor, Asian Institute of Technology (AIT), Bangkok, Thailand
2003 Professor, Department of Urban Environment Systems, Chiba University

Selected Publications:
• W. Liu and F. Yamazaki, "Detection of Crustal Movement from TerraSAR-X intensity images for the 2011 Tohoku, Japan Earthquake," *Geoscience and Remote Sensing Letters*, Vol.10, No.1, pp. 199-203, 2013.
• A. Meslem, F. Yamazaki, and Y. Maruyama, "Accurate evaluation of building damage in the 2003 Boumerdes, Algeria earthquake from QuickBird satellite images," *J. of Earthquake and Tsunami*, Vol.5, No.1, pp. 1-18, 2011.

Academic Societies & Scientific Organizations:
• Japan Society of Civil Engineers (JSCE)
• American Society of Civil Engineering (ASCE)
• Seismological Society of America (SSA)
• Earthquake Engineering Research Institute, USA (EERI)



Name:

Wen Liu

Affiliation:

Assistant Professor, Graduate School of Engineering, Chiba University

Address:

1-33 Yayoi-cho, Inage-ku, Chiba 263-8522, Japan

Brief Career:

2010-2013 Ph.D. of Engineering, Chiba University

2013-2014 JSPS Postdoctoral Fellowship for Foreign Researchers, Tokyo Institute of Technology

2014- Assistant Professor, Graduate School of Engineering, Chiba University

Selected Publications:

- “Extraction of Tsunami Flooded Areas and Damaged Buildings in the 2011 Tohoku, Japan Earthquake from TerraSAR-X Intensity Images,” Earthquake Spectra, ERRI, Vol.29, No.S1, pp. S183–2000, 2013.

Academic Societies & Scientific Organizations:

- Japan Society of Civil Engineers (JSCE)
 - Remote Sensing Society of Japan (RSSJ)
 - Institute of Electrical and Electronics Engineers (IEEE)
-